Eur. Phys. J. E (2017) **40**: 32
DOI 10.1140/epje/i2017-11515-7

THE EUROPEAN PHYSICAL JOURNAL E

Regular Article

Numerical insights into the phase diagram of p-atic membranes with spherical topology*

A.G. Hansen[1], N. Ramakrishnan[2], P.B. Sunil Kumar[3], and J.H. Ipsen[1,a]

[1] MEMPHYS, Department of Physics, Chemistry, and Pharmacy, University of Southern Denmark, 5230 Odense M, Denmark
[2] Department of Bioengineering, University of Pennsylvania, Philadelphia, PA 19104, USA
[3] Department of Physics, Indian Institute of Technology Madras, Chennai 600036, India

Received 12 August 2016 and Received in final form 12 January 2017
Published online: 23 March 2017

Abstract. The properties of self-avoiding p-atic membranes restricted to spherical topology have been studied by Monte Carlo simulations of a triangulated random surface model. Spherically shaped p-atic membranes undergo a Kosterlitz-Thouless transition as expected with topology induced mutually repelling disclinations of the p-atic ordered phase. For flexible membranes the phase behaviour bears some resemblance to the spherically shaped case with a p-atic disordered crumpled phase and p-atic ordered, conformationally ordered (crinkled) phase separated by a KT-like transition with proliferation of disclinations. We confirm the proposed buckling of disclinations in the p-atic ordered phase, while the expected associated disordering (crumpling) transition at low bending rigidities is absent in the phase diagram.

1 Introduction

The properties of fluid membranes with in-plane orientational degrees of freedoms have been an active research field since the earliest theoretical studies of membrane-protein interactions in the 1970s. The fact that the membrane can serve as a mediator between proteins embedded in the membrane was recognised by Marcelja [1] and how the anisotropy of the membrane components can affect the cooperative transitions in the membrane was discussed by Nagle [2]. Lateral anisotropic shapes are common among membrane components and membrane inclusions, *e.g.* many low temperature phases of membranes have tilted lipid conformations and membrane proteins are often formed as p similar or identical sub-units forming characteristic shapes with C_{vp} symmetry in the plane. The cooperative behaviour of such membrane systems and their interplay with the membrane shapes have been studied for a range of systems, *e.g.* chiral ribbons [3], membranes with gemini lipids [4] and liquid crystalline polymersomes [5]. The effects of such anisotropic membrane components have received renewed attention with the identification of whole families of membrane proteins with membrane shape remodelling capacity, *e.g.* BAR-proteins, pathogenic toxins and reticulons. It is characteristic for these proteins that they are regularly shaped in the plane of the membrane, weakly interacting and some lateral association between them is required for shape deformation. This suggests that their physical properties must be understood in the language of liquid crystalline behaviour at a flexible interphase. Some questions on the relation between in-plane liquid crystalline ordering and membrane conformations were already addressed in 1980s and 1990s by analytical approaches in the context of membranes with hexatic ordering of its lipid positional degrees of freedoms or lipid tilt orientation or the corresponding smectic B or smectic C liquid crystals [6]. p-atic membranes were introduced in theoretical membrane modelling as a generalisation where the in-plane orientational order parameter is invariant under rotations with the angle $\phi \rightarrow \phi + \frac{2\pi}{p}$, for integer p. The relevant order parameter field is a symmetric, traceless tensor of order p, a generalisation of the well-known Q-tensor $\mathsf{Q} = Q(\hat{m} \otimes \hat{m} - \frac{1}{2}\mathsf{I})$ for nematic liquid crystals ($p = 2$), where $\hat{m}$ is a unit director [6]. In 2D all such tensors can be represented as a unit director and the magnitude of the tensor, in analogy with the nematic tensor Q. Membranes with p-atic ordering are thus expected to display common physical properties. The theoretical studies of p-atic membranes gave rise to many interesting predictions, which unfortunately have been out of reach to test experimentally. In this paper we carry out computer simulations of self-avoiding membranes with spherical topology. An attempt is made to compare our results with the theoretical predictions. The paper is organized as follows. In sect. 2 we introduce the simplest sub-

* Supplementary material in the form of .mp4 and .pdf files available from the Journal web page at
http://dx.doi.org/10.1140/epje/i2017-11515-7

[a] e-mail: ipsen@memphys.sdu.dk

class of continuum models of p-atic membranes (sect. 2.1) and some main results from the literature on the subject are summarised (sect. 2.2). The discretised description of p-atic membrane is given in sect. 3 along with their implementation on Dynamically Triangulated Surfaces (DTS) and analysis by Monte Carlo simulation. The results of the simulations and discussion of them are presented in sect. 4. First we consider the case of a membrane with a spherical shape in sect. 4.1, and then the extension to flexible membranes in sect. 4.2. Aspects of the ordered phase are described in sect. 4.3 and the membrane conformations around point disclinations are covered in sect. 4.4. Section 5 is for concluding remarks.

2 Models of p-atic membranes

Our understanding of the properties of p-atic membranes originates mainly from the analysis of continuum elastic models, which will be introduced in sect. 2.1, while some of the previous results, which have motivated this work are presented in sect. 2.2.

2.1 Continuum models

A continuum description of p-atic membranes has its starting point in Helfrich's free energy expression for the curvature elasticity of a fluid membrane [7]. The conformations of a closed membrane with area A, and local mean and Gaussian curvatures H and K, respectively, is governed by the energy functional

$$\mathcal{H}_{\mathrm{Hel}} = \frac{\kappa}{2}\oint_A \mathrm{d}A\,(2H - C_0)^2 + \frac{\bar{\kappa}}{2}\oint_A \mathrm{d}A\,K. \qquad (1)$$

The material parameter C_0 is the spontaneous (preferred) curvature of the membrane and κ is the bending elastic constant and has the dimension of energy. In eq. (1), we have neglected any contributions due to surface tension since we are only interested in fluid free standing membranes. As a consequence of the Gauss-Bonnett theorem [8], the integral of the Gaussian curvature K over the entire surface is a topological invariant with a value $2\pi\chi$, where χ is the Euler characteristic of the surface. Hence the second term in eq. (1) is a constant and therefore irrelevant for the energetics of membrane surfaces with fixed topologies. However, in the case of membranes with a p-atic in-plane order, it should be noted that the Gaussian curvature K can play an important role by coupling to the texture of the in-plane orientational field.

In the continuum description, an in-plane p-atic field is represented by the unit vector $\hat{m}$, with $\hat{m}$ being invariant upon rotations of $2\pi n/p$, where n is a positive integer. The in-plane texture of $\hat{m}$ is governed by the local gradients through the energy functional [9]

$$\mathcal{H}_m = \frac{K_A}{2}\oint_A \mathrm{d}A\,(\nabla\hat{m})^2. \qquad (2)$$

Here, K_A is the elastic stiffness parameter of the p-atic field $\hat{m}$ with the dimension of energy. $\nabla_{\boldsymbol{q}}\hat{m}$ is the covariant derivative of $\hat{m}$ which is operating in the tangent plane of the membrane and measures the deviation from parallelism of $\hat{m}$ as we move along the tangent vector $\boldsymbol{q}$. So, eq. (2) will at low temperatures favour local alignment of $\hat{m}$ into parallel orientations. But for a curved surface it is in general not possible to make the vectors in a neighbourhood all parallel. This is *e.g.* reflected in the non-commutative nature of $\nabla_{\boldsymbol{q}}$ and it causes a geometrical frustration of the ordered state on curved membranes inducing or leading to coupling between in-plane ordering and membrane conformations (see appendix A for description of the properties of $\nabla_{\boldsymbol{q}}$). Equation (2) is relevant for the more general class of p-atic membranes with in-plane anisotropic elasticity, which is invariant under rotation of its components by the angle $\frac{2\pi}{p}$ in the plane [10,11]. For the cases $p = 1$ (polar) and $p = 2$ (nematic) a more specific energy expression holds:

$$\mathcal{H}_{\mathrm{Frank}} = \frac{K_1}{2}\oint_A \mathrm{d}A\,(\mathrm{Div}(\hat{m}))^2 + \frac{K_3}{2}\oint_A \mathrm{d}A\,(\mathrm{Div}(\hat{m}^{\perp}))^2. \qquad (3)$$

This is the so-called Frank's elastic free energy for a nematic liquid crystal in 2D [12]. The elastic constants K_1 and K_3 have the dimensions of energy and $\hat{m}^{\perp}$ is the orthonormal complement of $\hat{m}$ in the local tangent plane. For the closed membrane eq. (3) reduces to eq. (2) when $K_1 = K_3 = K_A$.

Similarly, eq. (1) must in general be extended to include terms involving the directional curvature for $p = 1$ and $p = 2$ [11]. In this work we will limit the analysis to the contributions of eq. (1) and eq. (2) to the total free energy. Further, we will restrict to the case $C_0 = 0$, to compare with the bulk of theoretical works for this case.

2.2 Previous theoretical results

The effect of thermal fluctuations on membranes has received major attention in the early days of theoretical membrane research. By 1985 it was established that the conformations of a fluid phantom membrane would appear crumpled on length scales larger than its persistence length $\xi(\kappa) = a\exp(4\pi\kappa/3k_{\mathrm{B}}T)$ [13–15], where a is the mesoscopic cut-off length, a result which also holds for self-avoiding fluid surfaces [16,17]. These conformations differ from those observed for tethered membranes, in which phantom surfaces display a crumpling transition [18,19], while self-avoiding surfaces remain ordered even at large length scales [20]. In 1987 Nelson and Peliti [21] and David, Peliti, and Guitter [22] addressed the question of the conformation of membranes with in-plane liquid crystalline order, exemplified with hexatic membranes. It was argued from the results of perturbative renormalisation group analysis to lowest order in $k_{\mathrm{B}}T/\kappa$ and $k_{\mathrm{B}}T/K_A$ that the conformational fluctuations of the membrane have no effect on the Kosterlitz-Thouless transition point $K_{\mathrm{KT}}/k_{\mathrm{B}}T = 2p^2/\pi$ [23]. In the following we set $k_{\mathrm{B}}T = 1$ to simplify notations. For $K_A \geq K_{\mathrm{KT}}$ the in-plane field

on the membrane remains orientationally ordered with no renormalisation of K_A. Further, it was also predicted that the bending rigidity κ renormalises to $\kappa_c(K_A) = K_A/4$ at long length scales and it remains rigid with no crumpling. For $\kappa > \kappa_c(K_A)$ the membrane appears rigid on short scales and softens to $\kappa_c(K_A)$ on long length scales, while for $\kappa < \kappa_c(K_A)$ the membrane appears softer on short length scales. This is the *crinkled* phase [22] of the membrane, which has infinite persistence length with the correlation between surface normals separated by a distance s are predicted to decline with a power law $s^{-\eta}$ for self-intersecting membranes, with $\eta = \frac{2}{\pi K_A}$. However, self-avoidance may turn the crinkled membrane asymptotically flat [22] similar to the crumpled phase of fixed connectivity membranes [20,24].

All the results described above are based on the analysis of quasi-planar, infinite membranes, where the p-atic ordered state can be considered to be disclination free. However, free-standing membranes in experimental systems are in general closed, with more or less complex topologies, and the p-atic ordered state is expected to have point disclinations imposed by the topology of the membrane. Lubensky and Prost [25] have investigated the texture and energetics of p-atic orientational order on a spherical membrane by theoretical analysis with several interesting conclusions. First, it was shown that for p-atic ordering the disclination will appear with the lowest possible index $\pm 1/p$, since higher disclinations with indices $\pm n/p$, $n \geq 2$ are energetically unfavored and will decay to n disclinations with index $\pm 1/p$. It is required by the Poincaré-Hopf theorem that the total disclination index is equal to χ, the Euler characteristic of the membrane. Thus, for a spherical membrane ($\chi = 2$) with p-atic order, $2p$ disclinations with index $+1/p$ are expected. Furthermore, it was argued that these point disclinations strongly repel each other with an energy

$$E = 2\pi K_A \left(2\ln\left(\frac{2R}{a}\right) - 1 - \frac{1}{2p^2}\sum_{i,j}^{2p} \left| \ln\left(\frac{2R\sin(\theta_{ij})}{a}\right)\right| \right) \tag{4}$$

that resembles 2D Coulomb interactions between charges of strength $1/p$. Here R is the radius of the sphere, θ_{ij} is the spherical angle between the disclinations i and j and $2R\sin(\theta_{ij})$ is the length of the chord between them. The problem of minimising eq. (4) is thus related to maximising the distance between the $2p$ disclination points on a sphere. This problem has been studied since J.J. Thomson's model of the atom of 1904 [26]. Unfortunately, no general analytical solution has been found, but numerical solutions for all the positions with $p \leq 400$ are available [27].

In general, p-atic membranes are not expected to be confined to spherical shapes. Nelson and Peliti [21] argued in 1987 that the disclination and dislocations energies are reduced by buckling of the membrane out of the plane. For disclinations the cone-shaped or saddle-shaped deformations are formed for $\kappa < \kappa_b = \frac{2p-1}{2p^2} K_A$ [28,21, 29] which may induce proliferation of disclinations, *i.e.* melting, at low κ for all K_A [29]. The shape of buckled p-atic membranes in the vicinity of the disclinations has also been studied in a mean-field setting [30] and more recently for tense p-atic membranes which deform into pseudo-spheres [12,31]. A more comprehensive RG analysis of the p-atic membrane, which includes these effects, was performed by Park and Lubensky [32–34] based on the descriptions given by Guitter and Kardar [29]. The crinkling line of fixed points became the solution of the equation $\kappa_c = \bar{K}_A(K_A, \kappa_c)/4$ terminating in the melting/crumpling fixed point at $\bar{K}_A^c = 2p^2/\pi$. Here, the effective stiffness $\bar{K}_A$ is given by

$$\bar{K}_A = K_A - \frac{3}{32\pi}\left(\frac{K_A}{\kappa}\right)^2, \quad \frac{3}{32\pi}\frac{K_A}{\kappa^2} \ll 1. \tag{5}$$

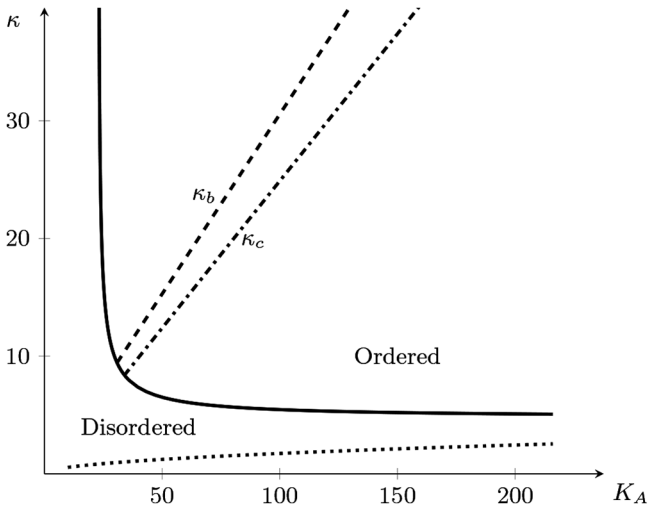

Fig. 1. Analytical phase diagram for $p = 6$ based on [32]. The solid line separates the ordered and the disordered phases, while the dash-dotted line is the line of fixed points for the crinkling transition, for which $\kappa_c = K_A/4$. The dashed line indicates the buckling transition and the dotted line indicates the lower limit of κ for the validity of eq. (5). The corresponding phase diagrams for other values of p are given in SI-1 and SI-2.

In this approach the melting/crumpling of p-atic membranes can be described by a single mechanism. The obtained phase diagram [32] is shown in fig. 1 (see also, Supplementary Material: SI-1 and SI-2).

3 Triangulated surface model

A triangulated surface is a closed, piece-wise flat surface constituted of $2(N - \chi)$ triangles that intersect in N vertices and $3(N - \chi)$ edges. This model establishes a framework to discretise the continuum models as described in sect. 2.1 for numerical studies of cooperative properties of membranes in the mesoscopic and macroscopic length scales. In our implementation of the triangulated surface model, all the surface properties are associated with the vertices. We denote the surface position and normal at a

vertex i by $\boldsymbol{X}_i$ and $\boldsymbol{N}_i$, respectively. The curvature properties in the neighbourhood of the vertex i are described by the discrete shape operator S_i, which may be obtained numerically. It is represented as a symmetric 2-tensor in the tangent plane TP_i and the eigenvalues of S_i are the local principal curvatures $c_1(i)$ and $c_2(i)$. The principal directions and the local surface normal form a local orthonormal frame of reference (Darboux frame). The details of the calculation of the discrete shape operator are given in [35]. The discretised form of the Helfrich's free energy eq. (1) based on the local discrete curvature invariants $2H_i = c_1(i) + c_2(i)$ and $K_i = c_1(i)c_2(i)$ takes the form

$$\mathsf{H}_{\mathrm{Hel}} = \sum_{i=1}^{N} A_i \left[\frac{\kappa}{2} (2H_i)^2 + \frac{\bar{\kappa}}{2} K_i \right]. \tag{6}$$

A_i is the vertex area constituted by a third of the area of the triangles shared by the vertex i. The identification of TP_i and the Darboux frame allows us to define the local unit director $\hat{m}_i \in TP_i$ at a vertex in order to represent the local orientation of an in-plane vector field. The implementation of the continuum in-plane elastic model eq. (2) on the triangulated surface requires a discrete representation of the covariant differentials. This was made possible with the discrete parallel transport between neighbouring vertices introduced in [35]. The generalised lattice XY-model for a p-atic in-plane field on a random triangulated surface takes the form

$$\mathsf{H}_m = -\frac{\varepsilon}{2} \sum_{\langle ij \rangle} (1 - \cos(p\phi_{i,j})), \tag{7}$$

where $\phi_{i,j}$ is the angle between neighbouring fields $\hat{m}_i$ and $\hat{m}_j$ after parallel transport. Equation (7) is thus invariant under local rotations of $\hat{m}_i$ by angle $2\pi/p$. In the low-temperature approximation eq. (7) corresponds to eq. (2) with $K_A \simeq \tilde{K}_A = \frac{\sqrt{3}}{2}\varepsilon p^2$.

The self-avoidance of the surface is ensured by assigning a hard core spherical bead of unit diameter to each vertex and a maximal tether distance of $\sqrt{3}$. This is not sufficient to impose strict self avoidance [17], but a mild constraint on the dihedral angle between two faces sharing a tether ensures self avoidance.

The Boltzmann probability distribution function

$$p(\{\boldsymbol{X}(i), \hat{m}(i)\}_{i=1}^{N}) \propto \exp\left(-\left(\mathsf{H}_{\mathrm{Hel}} + \mathsf{H}_m\right)\right) \tag{8}$$

is sampled using the Dynamically Triangulated Monte Carlo (DTMC) scheme, as described in [35]. Previously, melting transitions in hexatic membranes had been studied by Kroll and Gompper using the triangulated surface model [36]. In their approach the hexatic stiffness K_A was indirectly tuned by changing the maximal tether length between neighbouring vertices.

All the results presented in the following section were obtained using DTMC simulations for a triangulated surface of spherical topology, with $N = 2030$ vertices. A typical simulation (that includes both equilibration and production) is performed for 1×10^5 MCS for stiff membranes and for 4×10^6 MCS when the membrane is flexible. Here, MCS denotes a Monte Carlo step which is constituted of N orientational updates, N attempted vertex moves, and $3(N-2)$ attempted link flips (see [35] for details). All reported measures are thermodynamic averages obtained by averaging over at least 16 independent ensembles.

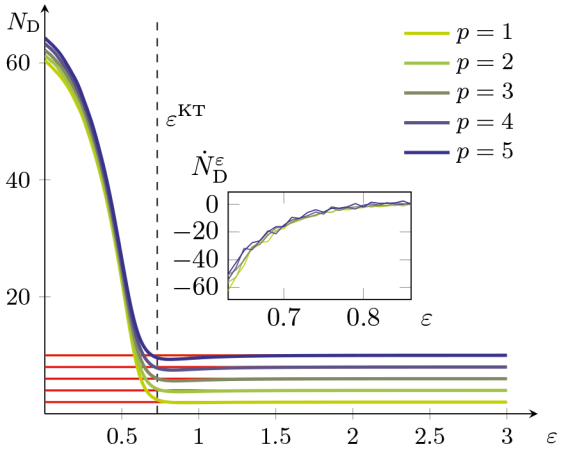

Fig. 2. Number of disclinations (N_{D}) on a sphere with 2030 vertices for p-atic fields with $p = 1, 2, 3, 4$, and 5. The horizontal lines correspond to $2p$ for each value of p. The inset shows the numerical derivative of N_{D} with respect to ε, in which $\dot{N}_{\mathrm{D}}^{\varepsilon} \simeq 0$ at $\varepsilon \to \varepsilon^{\mathrm{KT}} = 0.73$ is indicated by the dashed line.

4 Results and discussion

The results of the computer simulations of a spherical shaped p-atic membrane are presented and compared with the theoretical estimates with emphasis on the phase behaviour and the properties of the p-atic ordered phase. This is used as the basis for a presentation of the results for the p-atic membrane with full conformational flexibility. The phase diagram of the p-atic membranes is further complemented with analysis of the micro-roughness of the membrane and buckling transitions of disclinations in the ordered phase.

4.1 p-atic ordering on a spherical surface

We first verify some of the known analytical results presented in sect. 2.2 for the organization of a p-atic in-plane field on a spherical membrane. This model has some resemblance with the planar lattice models, however, the constant curvature of the spherical membrane influence the coupling between nearest neighbours of the orientational field on the lattice.

The phase behaviour found is in accordance with the theoretical expectation, that the system undergoes a continuous transition with characteristics of a Kosterlitz-Thouless transition at $K_A^{\mathrm{KT}} \simeq \frac{2}{\pi}p^2$ corresponding to $\varepsilon^{\mathrm{KT}} \simeq \frac{4}{\sqrt{3}\pi} \simeq 0.73$. This is reflected in a dramatic increase in the number of disclinations, N_{D}, as shown in

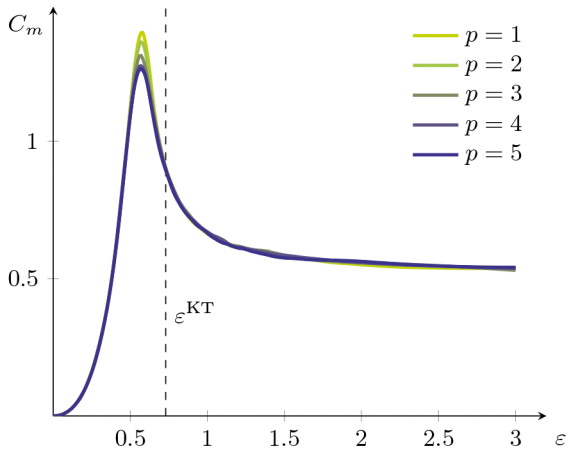

Fig. 3. Orientational specific heat for spherical systems with different values of p, calculated using eq. (10), the KT transition is indicated by the dashed line.

fig. 2 for $p = 1, 2, 3, 4, 5$. The inset in fig. 2 shows the numerical derivative of N_{D} with respect to ε, which shows an inflection near $\varepsilon^{\mathrm{KT}}$. In our simulations, a disclination is identified from the local discrete winding number

$$W(i) = \sum_{j \in C(i)} \phi_{j,j+1}, \tag{9}$$

where $\phi(j, j+1)$ is the angular difference (modulo $2\pi/p$) between neighbouring $\hat{m}_j$ and $\hat{m}_{j+1}$ after parallel transport of $\hat{m}_{j+1}$ along the closed path $C(i)$ constituted by the one-ring neighbourhood of vertex i. The associated index is given by $q_i = W(i)/(2\pi)$ except for a small correction from the local Gaussian curvature. This technique to compute N_{D} is highly effective if the surface is smooth and p is not too high.

The specific heat is another useful quantifier of a cooperative transition, which can readily be calculated from the fluctuations in the energy of the orientational field as

$$C_m = \frac{1}{N} \left(\langle \mathsf{H}_m^2 \rangle - \langle \mathsf{H}_m \rangle^2 \right). \tag{10}$$

Figure 3 shows the specific heat of the p-atic field as a function of ε, for $p = 1, 2, 3, 4, 5$. The profile of C_m is similar to the universal form seen for the KT transition of the planar XY-model [9] and the peak position ($\tilde{\varepsilon}$) is shifted slightly compared to the transition point. Furthermore, the p-dependence of the peak position, profile, and system size is very weak.

In the ordered phase for $\varepsilon > \varepsilon^{\mathrm{KT}}$ the spherical topology imposes $2p$ disclinations situated close to maximal distances from each other as shown in fig. 4 for snapshots of equilibrated systems with $\varepsilon = 10$ and $p = 1, 2, 3, 4$. Our observations are in good agreement with previous theoretical predictions [25] and also with simulations of in-plane nematic fields ($p = 2$) on a spherical surface [37]. A quantitative verification of the description of Prost and Lubensky [25] is shown in fig. 5 where the measured energy of the p-atic field by thermal averages of eq. (7) for the range

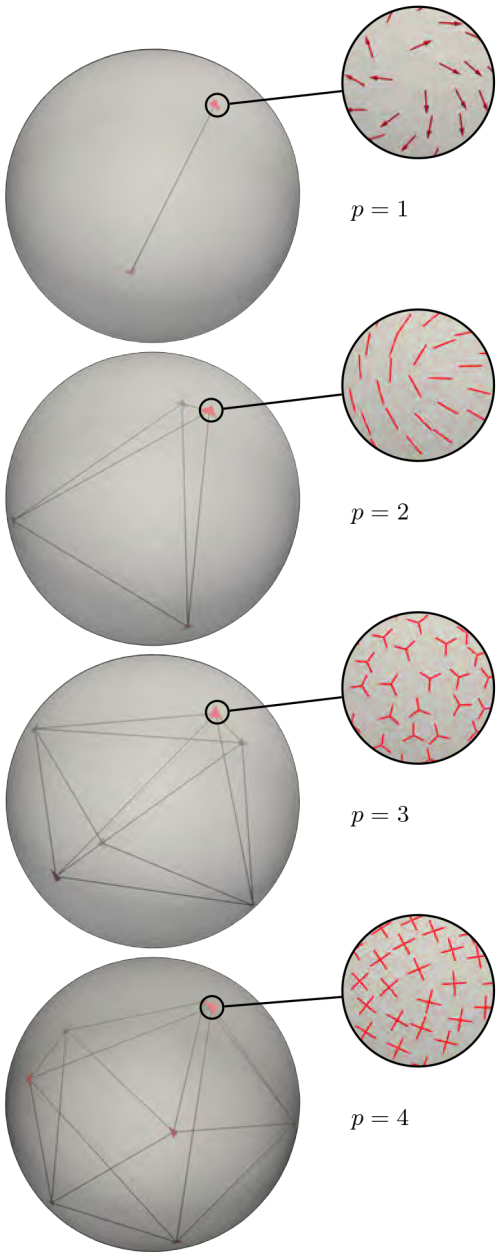

Fig. 4. Snapshots of the $2p$ p-atic disclinations and their locations for ordering fields, with $p = 1, 2, 3$, and 4, obtained for $\varepsilon = 10$. The disclinations position themselves at the corners of a digon, *i.e.* poles ($p = 1$), tetrahedron ($p = 2$), octahedron ($p = 3$), and square antiprism ($p = 4$).

of $p \in [1, 20]$ and $\varepsilon = 10$ for different N is shown. The corresponding theoretical values of the internal energy based on eq. (4) with maximal disclination distances are shown as full curves [25].

4.2 Phase diagram for flexible p-atic membrane

In this section the effect of p-atic ordering on a flexible membrane is investigated. Unlike for a p-atic field on stiff membranes, where the membrane phase diagram is only

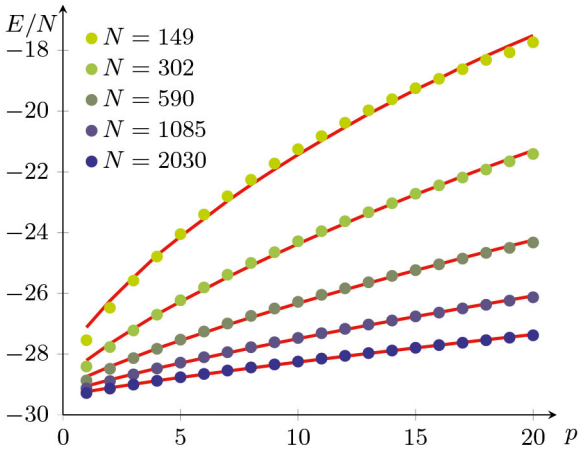

Fig. 5. Self interaction energy density for p-atic fields on a spherical membrane with $N = 149, 302, 590, 1085$, and 2030 vertices, for a self interaction strength of $\varepsilon = 10$. The symbols correspond to values computed from numerical simulations using the triangulated surface approach and the solid lines are estimates from eq. (4). E/N for $1 < p < 40$ are shown in SI-4 for $N = 77, 149$, and for $1 < p < 2000$ for all other values of N are shown in SI-5.

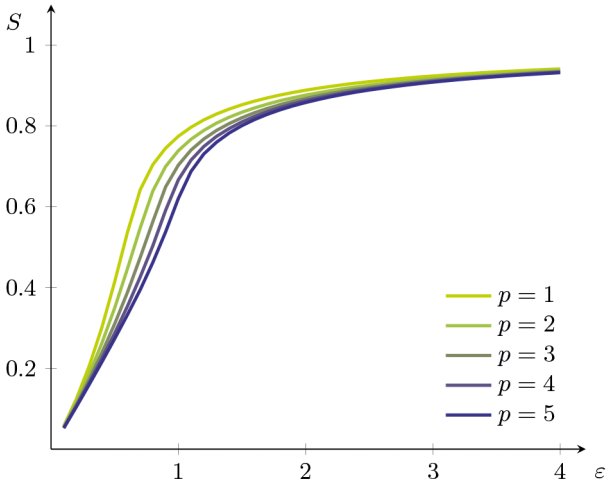

Fig. 6. S as function of ε for different values of p and $\kappa = 0.5$, see SI-19 for $\kappa = 0$ and $p = 1, 7$.

governed by the ordering state of the field, those on flexible membranes show a more complex spectrum of states that result from the interplay between in-plane ordering degrees of freedoms and membrane configurational degrees of freedoms. Overall, the obtained ε-κ phase diagram, fig. 7, consists of two regions, similar to the spherical p-atic surface discussed above.

The phase diagram is characterised from the local maxima of the overall specific heat (see SI-17) which is found by combining C_m (eq. (10)) and $C_{\rm Hel}$, where

$$C_{\rm Hel} = \frac{\langle \mathsf{H}_{\rm Hel}^2 \rangle - \langle \mathsf{H}_{\rm Hel} \rangle^2}{N} \,. \tag{11}$$

The similarity with the stiff spherical membranes is particularly striking for large κ values where the p-atic disordering transition point is close to $\varepsilon^{\rm KT}$ as found in sect. 4.1 (see fig. 3). This picture is confirmed by analyzing the p-atic nearest neighbor alignment parameter:

$$S = \frac{1}{6(N-2)} \left\langle \sum_{\langle i,j \rangle} \cos(p\phi_{i,j}) \right\rangle . \tag{12}$$

$S \simeq 1$ for the p-atic ordered state, while disordering gives $S \simeq 0$. S depends on ε as shown in fig. 6 for various p values. Within the ordered region S displays only minor variations with respect to κ (SI-18). The p-atic disordered region displays the same conformational behaviour as found in previous fluid membrane simulations with dynamically triangulated surfaces. At low κ values the membrane has the well-known branched polymer characteristics, while it appears quasi-spherical at high κ. In fig. 7 $\tilde{\kappa} \simeq 2.4$ respresents the position of a small cusp in $C_{\rm Hel}$ generally found in randomly triangulated surface simulations of fluid surfaces [16,17]. The nature of this transition or cross-over is still not resolved, but it corresponds to the lower limit of the rigid membrane regime with persistence length $\xi_p(\kappa)$ [17]. Interestingly, this cross-over continues into the p-atic ordered region (see SI-14–SI-16). The p-atic ordering transition shows a weak κ and p dependence

$$\tilde{\varepsilon} \simeq \begin{cases} \tilde{\varepsilon}_0, & \kappa \geq \tilde{\kappa}, \\ \tilde{\varepsilon}_0 + \dfrac{p-1}{27}(\kappa - \tilde{\kappa}), & \kappa < \tilde{\kappa}, \end{cases} \tag{13}$$

where $\tilde{\varepsilon}_0 \simeq 0.6$. The proximity of the $\tilde{\varepsilon}_0$ to $\varepsilon_{\rm KT}$ does not guarantee that the transition is a KT transition. However, the specific heat is hardly altered with system size for both high and low κ values (SI-21) It is interesting to note that the theoretical predictions of a low-κ crumpling transition (see sect. 2.2) seem not to be confirmed by this phase diagram.

4.3 The ordered phase

The high-ε region of the phase diagram ($\varepsilon > \tilde{\varepsilon}$) constitutes the ordered phase of the p-atic membrane. In fig. 7 some configurational snap-shots are shown for $p = 2$. A broader gallery of snap-shots from the p-atic ordered phase is shown in SI-22–SI-24 for $p = 1, 2, 3, 4, 5$ for $\varepsilon = 5, 10, 15$, and $\kappa = 0, 5, 10, 15, 20$.

Inspection of the textures of the p-atic field in the ordered state reveals that they have $2p$ disclinations distributed over the membrane surface, consistent with the theoretical predictions [25]. The disclinations are easily identified since the overall shapes of the membranes resemble distinct polyhedras as suggested by Prost and Lubensky [25] with the disclinations situated in the corners. However, as κ is increased the vesicle shapes will appear with more round corners (sect. 4.4) and the disclinations for such cases can be identified with the algorithm used for spherical surfaces (sect. 4.1). At large length scales the membrane appears ordered for $\varepsilon > \varepsilon^{\rm KT}$ independent

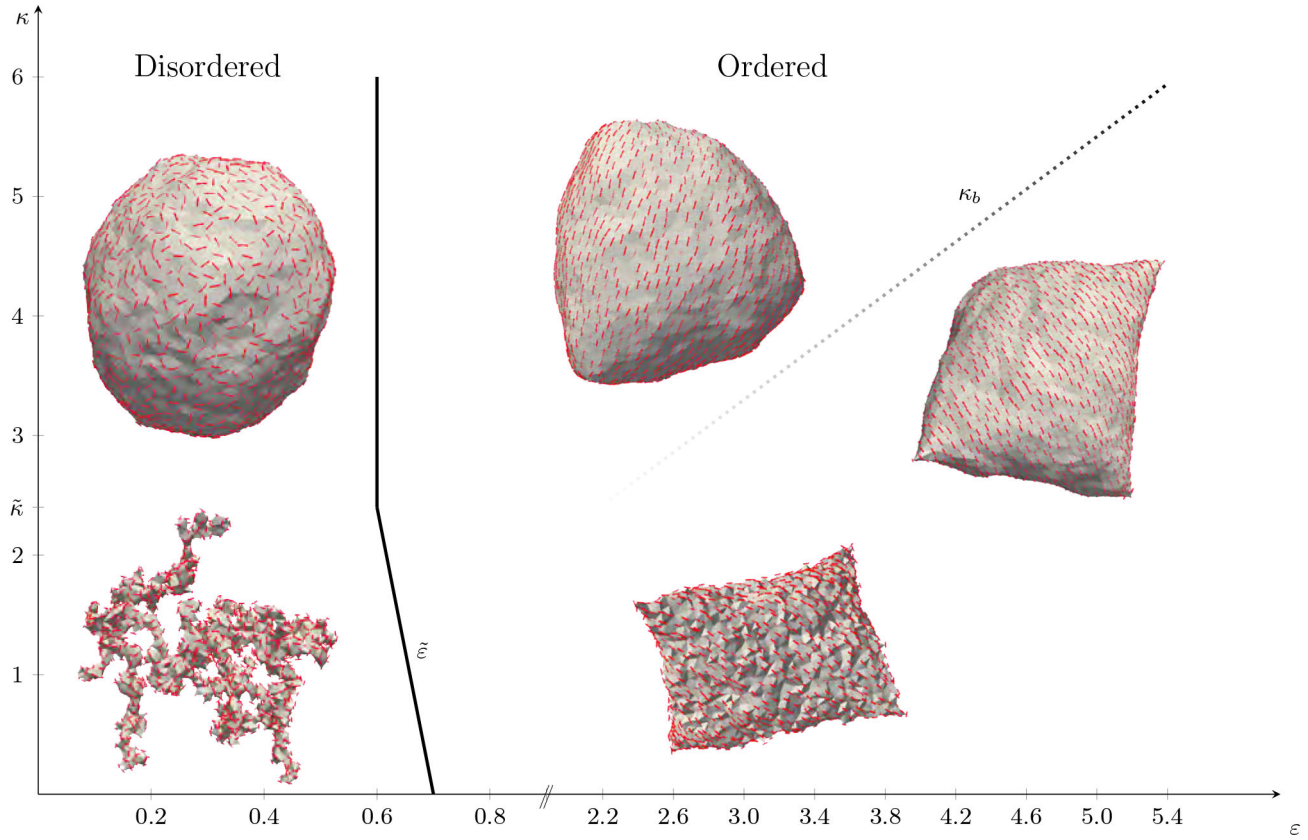

Fig. 7. Numerically determined phase diagram for a nematic in-plane field ($p = 2$) on a membrane of spherical topology, see SI-3 for different values of p. The solid curve $\tilde{\varepsilon}$, determined from eq. (10), denotes the order-disorder transition boundary for the nematic field. The dotted line is the buckling transition boundary based on analysis of curvature histograms. Note that there are two different scales on the ε-axis. The membrane conformations at various state points of this phase diagram may be found in the movie given as Supplementary Material.

of the choice of κ and p, while the short-scale behavior is varying.

For low κ values in the ordered phase the membrane is rough at short length scales, and gradually becomes more smooth with increase in κ. This is quantified by the vertex mean curvature distribution $P(H)$ shown in fig. 8. For most vertices the mean curvatures are Gaussian distributed around a mean value $\bar{H}$. Both $\bar{H}$ and the corresponding standard deviation $\sigma(H)$ are found to decrease with ε, p and κ (see SI-6). This tendency of $\bar{H}$ reflects that the overall configuration of the membrane becomes more ordered with increase in ε, p and κ. The shift in $\bar{H}$ is modest reflecting only slight modifications in the overall curvatures. For $\sigma(H)$ the change is dramatic (see SI-6), depending both on ε and p for small κ and collapsing into a $\kappa^{-\frac{1}{2}}$ (see inset of SI-6 and SI-7) relationship for large κ, as expected from the equipartition theorem for semi-flexible membranes. This behavior is consistent with the crinkled phase, where the effective bending rigidity at short distances is given by κ, while the bending rigidity for the large-distance conformations tends to $\kappa_c(K_A)$ [32]. A closer analysis shows that $\sigma(H)$ display approximative power law behavior in ε and p (see fig. 9 and SI-8, SI-9), which can be summarised in the phenomenological relation

$$\ln(\sigma(H)) \simeq \beta(\kappa) \ln(\tilde{K}_A) + \gamma(\kappa), \tag{14}$$

where $\beta(\kappa) \to 0$ and $\gamma(\kappa) \to -\frac{1}{2}\ln(\kappa)$ for κ large and $\beta(\kappa) \to \beta_0$ and $\gamma(\kappa) \to \gamma_0$ for $\kappa \to 0$, β_0 and γ_0 are some constants. Equation (14) thus represents a cross-over behaviour from the local flexible to rigid regimes of the ordered (crinkled) phase.

4.4 Shapes of disclinations in a p-atic ordered membrane

The theoretical arguments reviewed in sect. 2.2 suggests that an important ingredient for understanding the melting of p-atic ordered membranes is the buckling instability of membranes close to point disclinations of the p-atic field. In this section we analyse the buckling instability of the membrane in the ordered phase by use of the discretised model. We have previously shown configurations with disclinations bound to curvature singularity for $p = 1$ and $p = 2$ [35,38]. Similarly, the equilibrium configurations for all combinations of $p = 1, 2, 3, 4, 5$, $\varepsilon = 5, 10, 15$,

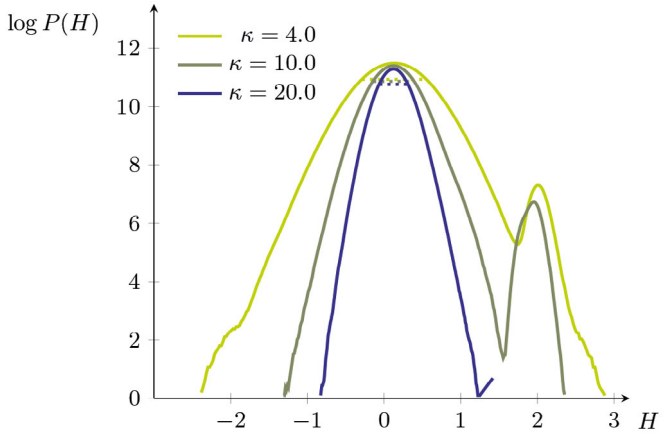

Fig. 8. Mean curvature distribution for different values of κ and $p = 4$, $\varepsilon = 10.0$. The dotted lines are the standard deviations of the main peaks fitted by a Gaussian distribution. The bimodal behavior of the distributions is caused by buckling of the membrane due to the presence of disclinations.

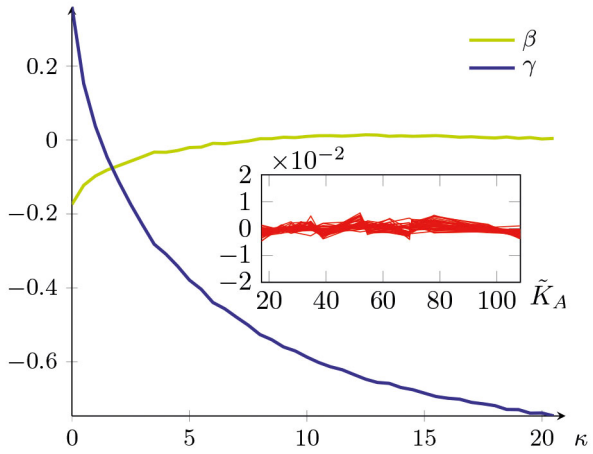

Fig. 9. Fit of the phenomenological model eq. (14). The inset shows the difference of l.h.s. and r.h.s. of eq. (14) after fitting, and emphasises the goodness of the fit. Slope of γ for $\kappa \in [9.5, 20.5]$ is -0.51.

and $\kappa = 0, 5, 10, 15, 20$ are shown in SI-18, SI-19, SI-20, where certain combinations show disclinations with associated curvature singularity in the membrane configurations. These high-curvature configurations are observable in the mean curvature distribution functions as a separate peak at high curvatures as shown in fig. 8. For each ε and p this peak vanishes at a buckling threshold $\kappa_b(\varepsilon, p)$ (see fig. 11). Another way to represent the mean curvature distribution is to form an ordered series of the mean curvatures for each snap shot and then successively average these series between all the snapshots as shown in fig. 10. In such a representation it appears that, below $\kappa_b(\varepsilon, p)$, the vertices with $2p$ disclinations leads to high-curvature branches (red lines) that are separated from the bulk (green area) of curvatures. $\kappa_b(\varepsilon, p)$ is indicated in the phase diagram (fig. 7). In general $\kappa_b(\varepsilon, p)$ is linear in ε:

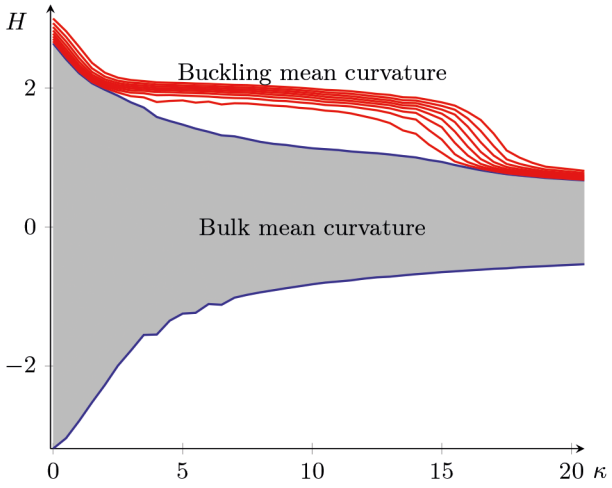

Fig. 10. Ordered mean curvature distribution and time averaged for each value of κ where $\varepsilon = 10, p = 5$. This representation is formed by ordering numerical values of the local mean curvatures for each snapshot followed by averaging each order across the snapshots. The red lines represent the vertices with $2p$ disclinations, having the highest local mean curvatures, while the gray area represents the rest of the local mean curvatures.

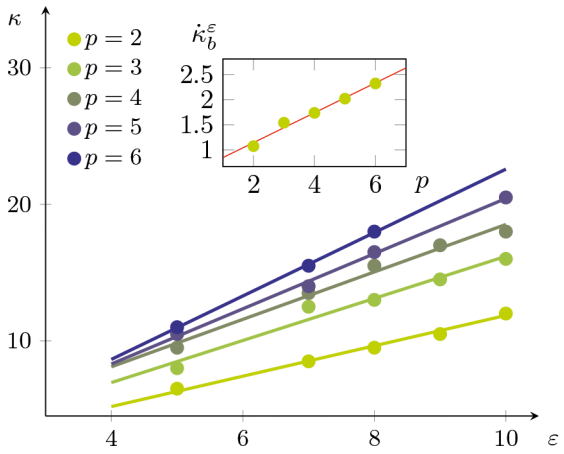

Fig. 11. Buckling transition for different values of p, the inset shows a simple linear relation between the slope of the buckling lines and p.

$\kappa_b(\varepsilon, p) \simeq \dot{\kappa}_b^{\varepsilon}(p)\varepsilon$ (fig. 11) supporting that a simple balance between the curvature energy and disclination energy is in play for the buckling transition [21,29]. This is furthermore supported by the finding that $\dot{\kappa}_b^{\varepsilon}(p) \simeq 0.3p + 0.5$ (inset of fig. 11). While the functional dependence of κ_b in ε and p are in agreement with the simple estimate $\kappa_b(K_A) \simeq \frac{2p-1}{p^2} K_A$ based on balancing the curvature energy and the disclination energy of a wedge-shaped buckling the coefficients are different. The membrane buckling is expected to partially screen the repulsive interactions between the disclinations [21]. This effect is not very clear from the simulation results since the equilibrium configurations always have well separated disclinations (SI-20).

5 Conclusions

We have investigated the phase behaviour of p-atic membranes in the κ-K_A parameter space using Monte Carlo simulation of self-avoiding triangulated surfaces. Overall, our results support the view that there are two phases separated by a line of transitions between the ordered (crinkled) phase and the disordered phase, which for high κ values coincides with the expected Kosterlitz-Thouless transition. However, in the low-κ regime the observed crumpling/melting transition deviates substantially from the theoretical expectation (fig. 1). In particular our results suggest that the ordered phase persists down to $\kappa = 0$. The origin of these differences can be manifold. The theoretically predicted phase diagram is based on a perturbative calculations for small $1/\kappa$ and $1/K_A$ so it may fail to capture the small κ behaviour of the continuum models. In particular for small p values the validity of the perturbative RG approach is questionable, since the obtained crumpling fixed point falls well above the small $K_A - K^{\mathrm{KT}}$ requirement ($\frac{3}{32\pi}\frac{K_A}{\kappa^2} \ll 1$). The discrepancies could also be due to the DTMC approach to simulating the surface. But one should keep in mind that though the DTMC approach has its limitations in modelling the surface at short scales, which may dictate the properties of the disclinations, the disclination energies are well captured by the discretised model for a spherical surface. Furthermore, the discrete model predicts the buckling of the membrane surface in the vicinity of a disclination as predicted by the continuum models. However, the buckling transitions found are significantly reduced compared to the theoretical estimate. Furthermore, the accompanying curvature-induced screening between disclinations, which is essential for the low-κ KT transition, are not observable in our simulations. Again, both approaches may fail to accurately describe the phenomena. For the numerical approach discretisation effects may play a role for the highly curved and p-atic ordered configurations close to the disclination cores. In the previous analytical description of membrane buckling induced by disclinations, cone-like configurations are assumed. This is probably a good approximation, however, recent numerical analysis of the corresponding free energy suggests that the equilibrium configurations rather resemble pseudo-spheres [39]. In their study free energy minimisation was only considered for $+\frac{1}{p}$ disclinations, which appear naturally for a spherical p-atic membrane. However, $-\frac{1}{p}$ disclinations are required for a KT-type transition. The associated buckled membrane configurations have been proposed to be saddle shaped, which gives rise to significantly higher disclination energies as compared to the $+\frac{1}{p}$ [28]. This leads to some problems in understanding the KT transition on a fluctuating surface. In particular the simple Kosterlitz-Thouless criterion [23] for melting based on free energy considerations for a single disclination fails and a more complex description of the disclination unbinding proces involving non-linear effects must be employed. It has been suggested to average the transition estimates obtained from Kosterlitz-Thouless criterion for $+\frac{1}{p}$ and $-\frac{1}{p}$ disclinations [40], or to replace the elastic constants with their renormalised values, which favours unbuckled disclinations on large scales [41], but a concise theory does not exist. Despite the found proximity of the p-atic disordering transition at DTMC to $\varepsilon_{\mathrm{KT}}$ and other similarities to a KT transion we cannot conclude that it is a KT transition, since the current finite size scaling analysis technology for DTMC is not sufficiently developed for this task and the accessible range of system sizes is limited. The ordered phase has properties resembling the predicted crinkled phase for membranes, *e.g.* we find that at low κ the ordered phase structure appears highly rough at short scales, comparable with the crumpled (fluid phase) at low K_A values, while the membrane becomes smooth at short scales as κ is increased. For system sizes considered, the crinkled phase appears conformationally ordered at long length scales. Both the self-avoidance and the repulsive disclinations imposed by the spherical topology may contribute to stabilise the long-range order of the membrane.

The authors would like to acknowledge the support from Human Frontier Science Program grant RGP0029-2014. The numerical results were made possible by the computing facilities at Danish Centre for Scientific Computing (Horseshoe), Danish e-Infrastructure Cooperation (ABACUS 2.0), and P.G. Senapathy Center for Computing Resource at IITM (Virgo).

Author contribution statement

A.G. Hansen made code development and conducted the Monte Carlo simulations and data analysis. N. Ramakrishnan and P.B. Sunil Kumar developed the basic triangulated surface code and contributed with project planning and data interpretation. J.H. Ipsen developed the basic triangulated surface code, planned the project, the data analysis and their interpretation and wrote the paper.

Appendix A. Properties of $\nabla_{\mathbf{q}}$

The covariant derivative $\nabla_{\boldsymbol{q}}$ is a generalisation of the Cartesian directional derivative. For the vector field $\hat{m}(\boldsymbol{X})$ on a surface locally parametrised with the surface position $\boldsymbol{X}$ and positions in its tangent plane $\boldsymbol{X} + \boldsymbol{q}$ it takes the form

$$\nabla_{\boldsymbol{q}}\hat{m}(\boldsymbol{X}) \simeq (T_{\boldsymbol{X}+\boldsymbol{q}\to\boldsymbol{X}}(\hat{m}(\boldsymbol{X}+\boldsymbol{q})) - \hat{m}(\boldsymbol{X}))/|\boldsymbol{q}|, \quad \text{(A.1)}$$

where $\boldsymbol{q} \in TP_{\boldsymbol{X}}$ and $T_{\boldsymbol{X}+\boldsymbol{q}\to\boldsymbol{X}}$ represents the parallel transport of tangent vectors from surface position at $\boldsymbol{X}+\boldsymbol{q}$ to $\boldsymbol{X}$. Details of its implementation on a discrete surface are described in [35,38,42].

$\nabla_{\boldsymbol{q}}$ gives rise to an indirect coupling to the curvature which is reflected in the non-commutative properties of $\nabla_{\boldsymbol{q}}$

$$[\nabla_{\boldsymbol{q}}, \nabla_{\boldsymbol{q}'}]\,\hat{m} = \det(\boldsymbol{q}, \boldsymbol{q}')K\hat{m}^{\perp}. \quad \text{(A.2)}$$

Equation (A.2) expresses that in a neighbourhood of a surface with non-vanishing Gaussian curvature succesive applications of $\nabla_{\boldsymbol{q}}$ along different directions $\boldsymbol{q}$ will lead to

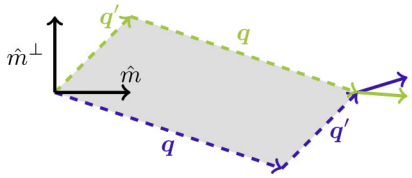

Fig. 12. Non-commutative actions by $\nabla_{\boldsymbol{q}}\nabla_{\boldsymbol{q}'}$ and $\nabla_{\boldsymbol{q}'}\nabla_{\boldsymbol{q}}$ on $\hat{m}$.

different results depending on the order of the differentiations (see fig. 12).

An elastic energy density (see eq. (2)) can be formed from $\nabla_{\boldsymbol{q}}$ similarly to the Cartesian case established from the trace obtained from the symmetric bilinear form $\nabla_{\boldsymbol{q}}\hat{m}\cdot\nabla_{\boldsymbol{q}'}\hat{m}$, which is given the short form $(\nabla\hat{m})^2$ in eq. (2).

References

1. S. Marčelja, Biochim. Biophys. Acta Biomembr. **455**, 1 (1976).
2. J. Nagle, Phys. Rev. Lett. **34**, 1150 (1975).
3. J.V. Selinger, F.C. MacKintosh, J.M. Schnur, Phys. Rev. E **53**, 3804 (1996).
4. M. Fošnarič, K. Bohinc, D.R. Gauger, A. Iglič, V. Kralj-Iglič, S. May, J. Chem. Inf. Model. **45**, 1652 (2005).
5. X. Xing, H. Shin, M.J. Bowick, Z. Yao, L. Jia, M.H. Li, Proc. Natl. Acad. Sci. U.S.A. **109**, 5202 (2012).
6. P.G. de Gennes, J. Prost, *The Physics of Liquid Crystals (International Series of Monographs on Physics)* (Clarendon Press, 1995).
7. W. Helfrich, Z. Naturforsch. C: Biochem. Biophys. Biol. Virol. **28**, 693 (1973).
8. M.P. do Carmo, *Differential Geometry of Curves and Surfaces* (Prentice Hall, Engelwood Cliffs, NJ, 1976).
9. P.M. Chaikin, T.C. Lubensky, *Principles of Condensed Matter Physics* (Cambridge University Press, Cambridge, 1995).
10. J.M. Park, T.C. Lubensky, F.C. MacKintosh, Europhys. Lett. **20**, 279 (1992).
11. L. Peliti, J. Prost, J. Phys. (Paris) **50**, 1557 (1989).
12. F.C. Frank, Discuss. Faraday Soc. **25**, 19 (1958).
13. P. De Gennes, C. Taupin, J. Phys. Chem. **86**, 2294 (1982).
14. W. Helfrich, J. Phys. (Paris) **46**, 1263 (1985).
15. L. Peliti, S. Leibler, Phys. Rev. Lett. **54**, 1690 (1985).
16. G. Gompper, D.M. Kroll, Phys. Rev. E **51**, 514 (1995).
17. J.H. Ipsen, C. Jeppesen, J. Phys. I **5**, 1563 (1995).
18. Y. Kantor, M. Kardar, D.R. Nelson, Phys. Rev. Lett. **57**, 791 (1986).
19. Y. Kantor, M. Kardar, D.R. Nelson, Phys. Rev. A **35**, 3056 (1987).
20. M. Plischke, D. Boal, Phys. Rev. A **38**, 4943 (1988).
21. D. Nelson, L. Peliti, J. Phys. (Paris) **48**, 1085 (1987).
22. F. David, E. Guitter, L. Peliti, J. Phys. (Paris) **48**, 2059 (1987).
23. J.M. Kosterlitz, D.J. Thouless, J. Phys. C **6**, 1181 (1973).
24. Y. Kantor, K. Kremer, Phys. Rev. E **48**, 2490 (1993).
25. T.C. Lubensky, J. Prost, J. Phys. II **2**, 371 (1992).
26. J. Thomson, Philos. Mag. Ser. 6 **7**, 237 (1904).
27. D.J. Wales, S. Ulker, Phys. Rev. B **74**, 212101 (2006).
28. H.S. Seung, D.R. Nelson, Phys. Rev. A **38**, 1005 (1988).
29. E. Guitter, M. Kardar, Europhys. Lett. **13**, 441 (1990).
30. C.M. Ghim, J.M. Park, J. Phys.: Condens. Matter **15**, 3891 (2003).
31. L. Giomi, Phys. Rev. Lett. **109**, 136101 (2012).
32. J.M. Park, T.C. Lubensky, Phys. Rev. E **53**, 2648 (1996).
33. J.M. Park, T.C. Lubensky, Phys. Rev. E **53**, 2665 (1996).
34. J.M. Park, Phys. Rev. E **54**, 5414 (1996).
35. N. Ramakrishnan, P.B.S. Kumar, J.H. Ipsen, Phys. Rev. E **81**, 041922 (2010).
36. G. Gompper, D.M. Kroll, Curr. Opin. Colloid Interface Sci. **2**, 373 (1997).
37. H. Shin, M.J. Bowick, X. Xing, Phys. Rev. Lett. **101**, 037802 (2008).
38. N. Ramakrishnan, P.B.S. Kumar, J.H. Ipsen, Macromol. Theory Simul. **20**, 446 (2011).
39. M.M. Taniguchi, F.C. Zola, V.G. Guimarães, G. Gonçalves, R. Rossato, R.S. Zola, Acta Sci. Technol. **36**, 663 (2014).
40. J.M. Park, T.C. Lubensky, J. Phys. I **6**, 493 (1996).
41. M.W. Deem, D.R. Nelson, Phys. Rev. E **53**, 2551 (1996).
42. J.H. Ipsen, Int. J. Adv. Eng. Sci. Appl. Math. **8**, 121 (2016).